PHYSICAL REVIEW B
CONDENSED MATTER

THIRD SERIES, VOLUME 41, NUMBER 11 15 APRIL 1990-I

Electronic structure of $Cu_{75}Au_{25}$ disordered alloy

E. Arola, R. S. Rao, and A. Salokatve
Department of Physics, Tampere University of Technology, SF-33101 Tampere 10, Finland

A. Bansil
Department of Physics, Northeastern University, Boston, Massachusetts 02115
(Received 14 April 1989; revised manuscript received 15 September 1989)

We present angle-resolved uv photoemission (normal emission) measurements from the (100) and (111) surfaces of $Cu_{75}Au_{25}$ alloy single crystals, together with fully relativistic as well as nonrelativistic Korringa-Kohn-Rostoker coherent-potential-approximation calculations of complex energy bands and densities of states. A good overall accord is found between the measurements and theoretical predictions with regard to the shifts and smearings of various bulk states in the alloy. The characteristic effects of alloying Au on the electronic structure of Cu are identified; the principal Au-induced feature is 2.5 eV wide, and appears 3 eV below the Cu-derived *d* band in the alloy; this feature is split into two distinct peaks, approximately 1.4 eV apart, due to relativistic spin-orbit interaction. The (111) Shockley surface state is observed to shift by 80 meV towards the Fermi energy in the alloy, and to suffer an increased broadening (full width at half maximum) of 140 meV compared with Cu.

I. INTRODUCTION

The bulk phase transition in Cu_3Au at 390 °C is a classic example of an order-disorder transformation. The electronic structure of this alloy is also an important touchstone for relativistic theories because Au is a heavy metal possessing strong spin-orbit interaction. Although Cu and Au are isoelectronic noble metals, the Au *d* band is much wider than that of Cu, and therefore the effective disorder parameter in the alloy is strongly **k** and *E* dependent, leading to large disorder effects in the electronic spectrum. Numerous studies of this system include optical reflectivity,[1,2] photoemission,[2-4] Hall constant,[5] magnetic susceptibility,[6] thermoelectric power,[6] thermal properties,[7] surface transitions,[8-10] surface segregation,[9,11-13] and surface core-level (Au) shifts.[14,15] Many band-structure calculations on the ordered Cu_3Au are available,[16-20] and experimental (angle-resolved photoemission) band structure has recently been determined.[3] The electronic structure of the disordered phases is less well studied, although a number of photoemission measurements and electronic structure calculations on $Cu_{75}Au_{25}$ and $Cu_{90}Au_{10}$ have been reported.[18,20-22].

In this article, we present fully relativistic Korringa-Kohn-Rostoker coherent-potential-approximation (KKR-CPA) calculations on disordered $Cu_{75}Au_{25}$ together with angle-resolved photoemission (normal emission) measurements from the (100) and (111) $Cu_{75}Au_{25}$ single-crystal surfaces using Ne I, He I, and He II unpolarized radiation. The usefulness of angle-resolved photoemission techniques in probing energy bands in perfect crystals, and more recently in disordered alloys, in **k**-point–by–**k**-point detail is well established.[22,23] Note that Bloch energy bands become complex in a disordered alloy, where the real and imaginary parts of levels give positions and widths of peaks in the spectral density function respectively; complex energy bands thus constitute a convenient representation of the spectrum of an alloy. An analysis of the positions of the spectral features in an angle-resolved photoemission experiment often permits a reasonable determination of the alloy spectrum. While further insight should be possible by comparing calculated and measured spectral intensities,[24] such a discussion is considered beyond the scope of this paper. This work extends our previous study[22] of $Cu_{90}Au_{10}$ alloys. Also, since we employ a fully relativistic theoretical approach, we are in a position to clearly identify relativistic effects in the electronic spectrum.

An outline of this paper, together with its principal conclusions, is as follows. Section II gives technical details of sample preparation, the construction of Cu and Au muffin-tin potentials, and related information. Sec-

tion III presents and discusses the angle-resolved measurements, the calculated complex energy bands, and the densities of states in the alloy. By comparing relativistic and nonrelativistic calculations, characteristic relativistic effects on the spectrum are identified.

Our meaurements and calculations show the following principal effects of alloying Au on the band structure of Cu: (i) The main Au-induced structure appears about 3 eV below the Cu-derived d-band complex, possesses a width of about 2.5 eV, and consists of two distinct spin-orbit split peaks; (ii) the top of the Cu-derived d-band complex in the alloy remains at almost the same energy as in Cu; (iii) the width of the Cu-related d band decreases with increasing Au concentration; and (iv) the disorder-induced smearing of the bulk states in the alloy is strongly $\mathbf{k}$ and E dependent, in substantial accord with measurements.

The (111) Shockley surface-state feature is observed in our experiments. By comparing this spectral feature in Cu and $Cu_{75}Au_{25}$, we deduce that the Shockley surface state experiences a shift of 80 meV towards the Fermi energy in the alloy, and an increased broadening [full width at half maximum (FWHM)] of about 140 meV.

Some aspects of our relativistic KKR-CPA approach are outlined in Appendixes A and B. While the methodology itself is not new,[24] we have implemented it in our group in order to study heavy-metal alloys, many of which possess important catalytic properties. In our treatment, we have considered both the Lloyd-type formulas[25] as well as the Green's-function-based formulas for the total and A (B) -site-decomposed component densities of states.[24] While we omit formal details for brevity, we note that the results for the total and component densities of states on the basis of the Green's-function and the Lloyd-type formulas were found to be virtually indistinguishable in the present alloy. The symmetry properties of the relativistic CPA scattering matrix are derived from a proper group-theoretical approach in Appendix A; seven linearly independent elements are found if only s, p, and d valence states are used. The form of the CPA scattering matrix (checked by explicit numerical evaluation of the relevant quantities) is similar to that presented in Ref. 24, except for sign changes in some of the elements. Finally, Appendix B outlines an effcient multidimensional Newton-Raphson formula for solving the CPA equation; we found this formula particularly useful for obtaining rapid convergence even in energy regimes where disorder effects are large.

It should be noted that the present measurements and calculations are consistent with previous relevant experimental and theoretical work[18,20–22]. Relatively smaller differences between various experiments are due perhaps to differences in sample preparation, resolution, and polarization of the radiation used. On the theoretical side, differences between various first-principles calculations arise primarily from those in the muffin-tin potentials used.

II. EXPERIMENTAL AND THEORETICAL CONSIDERATIONS

The experiments were performed using a multitechnique VG-ADES-400 spectrometer, with *in situ* facilities for low-energy electron diffraction (LEED), Auger-electron spectroscopy (AES), angle-resolved photoemission spectroscopy (ARPES), and x-ray photoelectron spectroscopy (XPS) measurements. He I (21.22 eV), He II (40.82 eV), and Ne I (16.85 eV) resonance lines from a gas-discharge lamp were used to produce electron emission. The sample preparation and handling methods used in the present work are similar to those used in our earlier studies of $Cu_{90}Au_{10}$ and other alloys.[22,23] Briefly, the (100) and (111) CuAu single crystals were grown by the Bridgman method. After mechanical and electrochemical polishing the samples were treated by repeated cycles of Ar^+-ion bombardment and annealing in order to obtain a good-quality surface. The crystal structure and the composition of the surface were monitored via LEED and AES measurements. At about 490 °C (100 °C above the bulk order-disorder transition temperature), AES studies indicate that the topmost surface layer contains about 30–40 at. % Au; our results in this regard are consistent with the conclusions of Ref. 11, and the surface-segegration studies on the $Cu_{75}Au_{25}(111)$ alloy surface.[13] The Au concentration in second and subsequent layers is expected to be close to the bulk value.[11] While LEED studies indicate that our samples possessed partial ordering in the surface region, we believe (judging from the intensity of the extra LEED spots) that the major part of the crystal is disordered, and that it is meaningful to compare the room-temperature measurements with the electronic structure calculations on the disordered phase.

Calculations reported in this article employ the fully relativistic KKR-CPA approach for treating the electronic structure of disordered alloys. The formal analysis of the mulitple-scattering equations in this case proceeds along the lines of the nonrelativistc theory[25–27] when proper bispinor states are chosen to represent the matrix elements of various operators. For example, complex energy bands in the alloy are obtained by solving the secular equation

$$\|\tau_{\mathrm{CP}}^{-1}-B(\mathbf{k},E)\|=0 ,$$

where τ_{CP} is the CPA scattering t matrix, and $B(\mathbf{k},E)$ is the matrix of relativistic KKR structure constants. Details of the formalism, including formulas for density of states, $\rho(E)$, and the A (B)-component density of states, $\rho_{A\,(B)}(E)$, are omitted in the interest of brevity.

Cu and Au muffin-tin potentials were obtained via the Mattheiss overlapping-charge-densities prescription, using $3d^{10}4s^1$ Herman-Skillman charge density for Cu, and $5d^{10}6s^1$ Liberman charge density for Au; full Slater exchange was employed. A fcc lattice of lattice constant 7.085 a.u. (the lattice constant of $Cu_{75}Au_{25}$ alloy) was used in the overlapping procedure. The Au potential so obtained was shifted rigidly to a lower energy with respect to the Cu potential by 0.089 Ry; as emphasized elsewhere,[23] this semiempirical adjustment may be viewed as a means of incorporating effects of charge rearrangement on the crystal potential in the alloy. A relatively minor downward shift of 0.017 Ry was also made in the Cu muffin-tin potential in order to obtain a better placement of the Cu d bands.

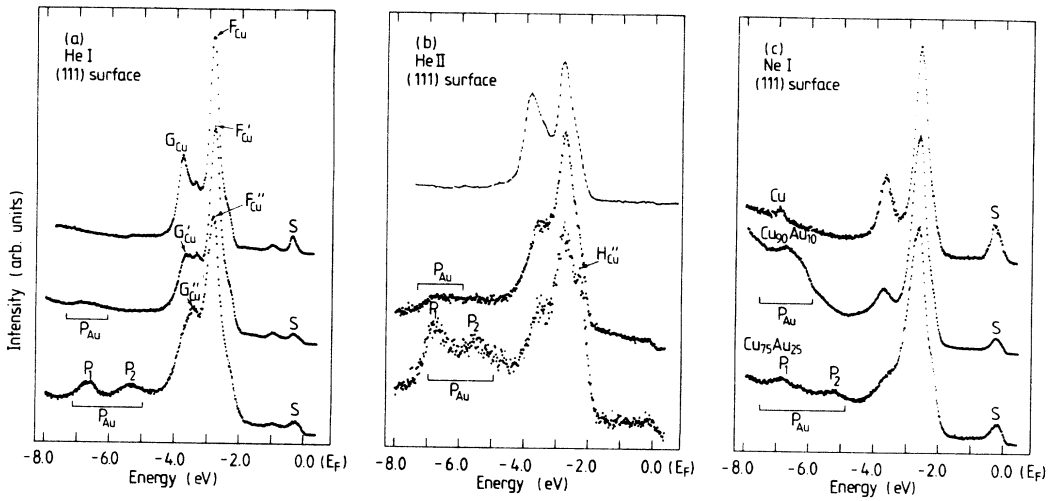

FIG. 1. He I, He II, and Ne I angle-resolved normal-emission spectra from the (111) surface of Cu (top set of curves), $Cu_{90}Au_{10}$ (middle set of curves), and $Cu_{75}Au_{25}$ (bottom set of curves). The Cu- and Au-related features, denoted by various letters, are discussed in the text.

III. RESULTS AND DISCUSSIONS

Ne I, He I, and He II excited normal-emission spectra from the (111) and (100) surfaces of $Cu_{75}Au_{25}$ single crystals are compared with those for pure Cu, and $Cu_{90}Au_{10}$ (Ref. 22) in Figs. 1 and 2. The **k** points corresponding to various distinct photoemission peaks were determined by assuming a free-electron final state (see Ref. 28).[29] Figure 3 compares the experimental $E_{\mathbf{k}}$ points so obtained with the calculated relativistic KKR-CPA complex energy bands along the $\Gamma-X$ and $\Gamma-L$ directions, and shows an excellent overall accord between theoretical predictions and measurements. In reference to this figure, the characteristic effects of alloying Au on the electronic structure of Cu may be identified as follows.

(i) The main Au-induced structure, with a width of about 2.5 eV in the 25% alloy (and 1.7 eV in the 10% alloy) denoted by P_{Au} in Figs. 1 and 2, appears 3 eV below the Cu-based d-band complex. The center of this broad structure in $Cu_{75}Au_{25}$ is at a somewhat lower binding energy (by about 0.7 eV) compared to $Cu_{90}Au_{10}$. This Au-induced structure consists of two distinct peaks P_1 and P_2, possessing little dispersion (less than 0.5 eV), which are centered at about -5.2 and -6.6 eV, respectively (Figs. 1 and 2). The lower peak P_1 is narrower and more intense compared to the upper peak P_2. These observations are consistent with the calculated Au density of states in Fig. 3(b), since for highly smeared bands, such as the Au bands in the alloy, density-of-states features are expected to be reflected even in angle-resolved spectrum. Note that the two aformentioned peaks are not clearly discernible in $Cu_{90}Au_{10}$ spectra. The presence of these two peaks is a characteristic relativistic spin-orbit-splitting effect; we return to this point below.

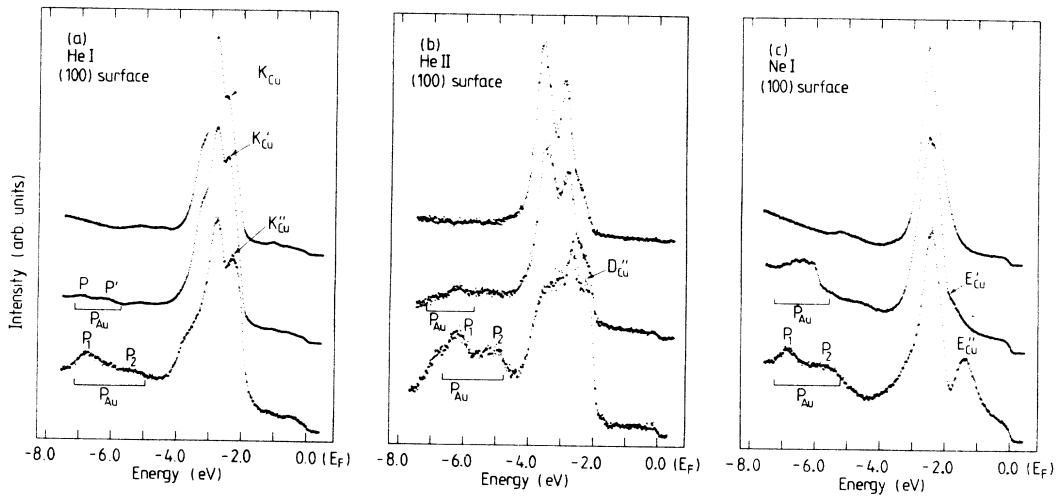

FIG. 2. Same as Fig. 1, except that this figure refers to the (100) surface.

(ii) The top of the Cu-derived d-band complex in the alloy remains at almost the same binding energy as in Cu. Note that the uv excitation energies used in this study do not probe the band structure at the symmetry points X or L; this feature may nevertheless be inferred from Fig. 3, since the energy bands near the top of the Cu d band (at X and L) are fairly flat and several measured E_k points lie in this energy region.

(iii) The width of the Cu-derived d-band complex in the alloy decreases with increasing Au concentration. This is expected because the number of like nearest-neighbor atoms decreases in the random phase upon alloying, and also the increase in the lattice constant causes the d-d overlap to decrease in the alloy. The value of the Cu bandwidth in $Cu_{75}Au_{25}$ (difference between the uppermost and lowest X_{7+} levels in Fig. 3) is 2.03 eV. The corresponding values in $Cu_{90}Au_{10}$ and Cu, are, respectively, 2.44 and 2.73 eV ($X_5 - X_3$, see Ref. 22).

(iv) Theory predicts a striking $\mathbf{k}$ and E dependence of disorder-induced smearing of levels in the alloy (shown by shading in Fig. 3). The top of the Cu-derived d band (e.g., upper X_{7+} or L_{4+} level) is essentially undamped, while the calculated smearing of, for example, the lowest X_{7+} level which marks the bottom of the Cu bands is about 0.4 eV. Note that the interpretation of the FWHM of photoemission peaks can be complicated when other nearby peaks are present; this is particulary the case for states near the bottom of the Cu bands which overlap with heavily smeared Au states.[30] Nevertheless, the predicted broadenings are found to be in good accord with measurements[31] in several cases. For example, increase in FWHM of the peak F''_{Cu} from that of F_{Cu}, which corresponds to emission from a level near the top of the Cu d band [see Figs. 1(a) and 3(a)], is about 230 meV, compared to the computed value of 270 meV. The most intense peak in the (111) Ne spectra, Fig. 1(c), is estimated to be broadened by 450 meV in the 25% alloy, compared to the theoretical value of 350 meV. In contrast, the most intense peak in the (100) Ne spectra, Fig. 2(c), hardly shows any increase in FWHM, and the computations correspondingly show a small smearing of about 30 meV.

It is noteworthy that the spectral intensity of the peak K_{Cu}, Fig. 2(a), is enhanced upon adding Au. This effect may be understood with reference to Fig. 3(b), which shows the presence of the peak A'_{Au} in the Au-component density of states. As a result, we would generally expect spectral features around 2 eV binding energy to be more enhanced in this alloy.

Relativistic effects on the electronic spectrum deserve further comment. In this connection, we have repeated calculations in $Cu_{75}Au_{25}$ using the nonrelativistic KKR-CPA theory with the present Cu and Au muffin-tin potentials; Figs. 4 and 5 summarize the relevant results. A comparison of relativistic and nonrelativistic component densities in Fig. 5(a) reveals the following major relativistic effects on the spectrum: (i) splitting of the Au-related

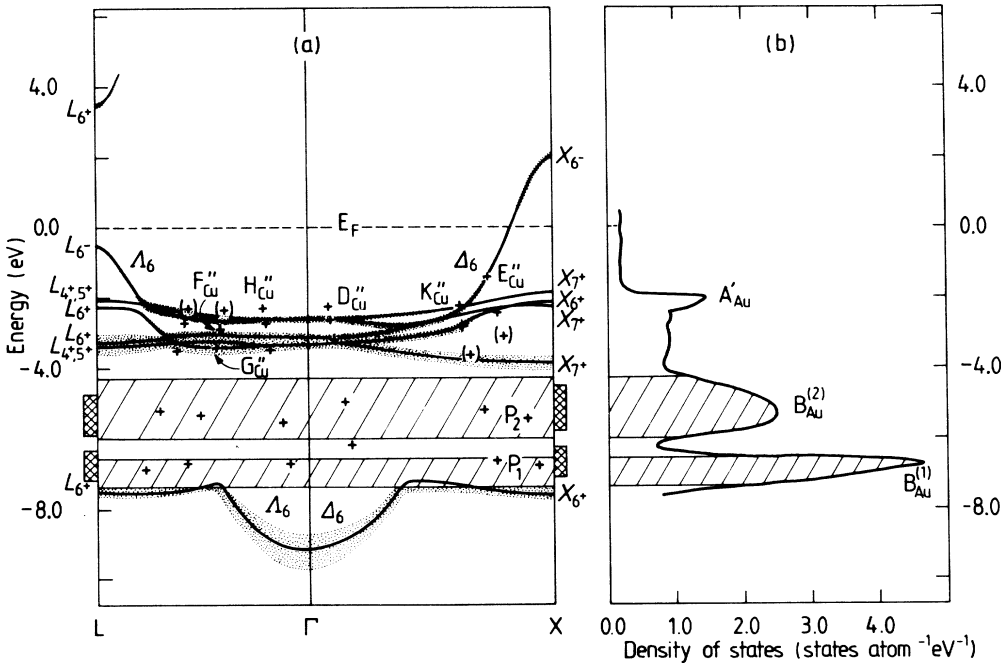

FIG. 3. (a) Relativistic KKR-CPA complex energy bands along the symmetry directions Γ–X and Γ–L, and (b) Au-component density of states in $Cu_{75}Au_{25}$. Disorder smearing of energy bands is represented by the vertical length of shading, which is twice the imaginary part of the complex energy. Heavily smeared Au-related d bands are shown in (a) by hatched regions of FWHM of the corresponding relativistically split peaks, $B^{(1)}_{Au}$ and $B^{(2)}_{Au}$, in the Au-component density of states in (b). Crosses denote the $E(\mathbf{k})$ values obtained from the experimental spectra (labels are keyed to the features of Figs. 1 and 2); parentheses indicate that the corresponding transitions in the spectra are seen only as shoulders. Cross-hatched regions on either sides of (a) estimate the average position and FWHM of the Au-derived structures in the ARPES spectra. Peak A'_{Au} in Au-component density of states is discussed in the text.

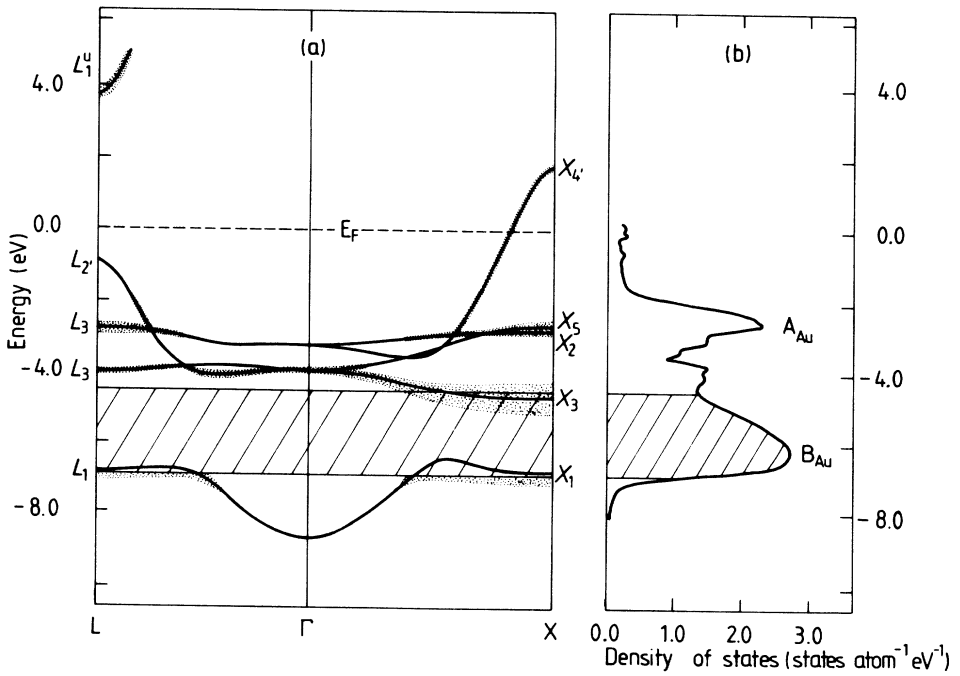

FIG. 4. (a) Nonrelativistic KKR-CPA complex energy bands along the symmetry directions $\Gamma-X$ and $\Gamma-L$, and (b) Au-component density of states in $Cu_{75}Au_{25}$. Cu and Au potentials used in these calculations are the same as those in the relativistic computations of Fig. 3.

nonrelativistic peak B_{Au} into two dinstinct peaks $B_{Au}^{(1)}$ and $B_{Au}^{(2)}$ ($B_{Au}^{(1)}$ and $B_{Au}^{(2)}$ originate predominantly from states of $d_{3/2}$ and $d_{5/2}$ symmetry, respectively); (ii) the Au peak A'_{Au} near the Cu band edge is reduced in intensity and moves to a somewhat lower binding energy (see A_{Au}); (iii) the Cu d-band complex moves to a lower binding energy. These changes in the spectrum upon including relativistic effects result in an increase in the overall width of the d band in the alloy; also, the separation between the main Cu- and Au-related densities is increased.

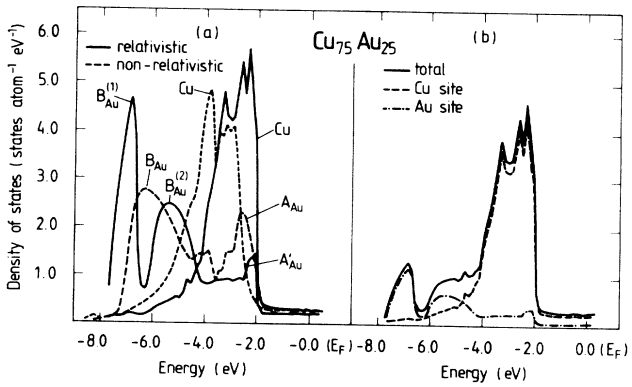

FIG. 5. (a) Cu- and Au-component density of states based on the nonrelativistic and the relativistic KKR-CPA scheme in $Cu_{75}Au_{25}$ (labels on peaks keyed to Figs. 3 and 4). (b) Relativistic KKR-CPA total and Cu (Au) component density of states; the component densities in (b) are the same as in (a), except they are weighted by the Cu (Au) concentration. All curves are drawn with respect to a common Fermi level.

Finally, comparing Figs. 3 and 4, marked differences between the relativistic and the nonrelativistic theory are also seen in the **k** dependencies of the disorder smearings of various complex bands. The good accord between theory and experiment, discussed with Fig. 3 above, indicates that the relativistic effects described in this paragraph are substantially verified by the present measurements.

Insight into the nature of the alloy electronic structure

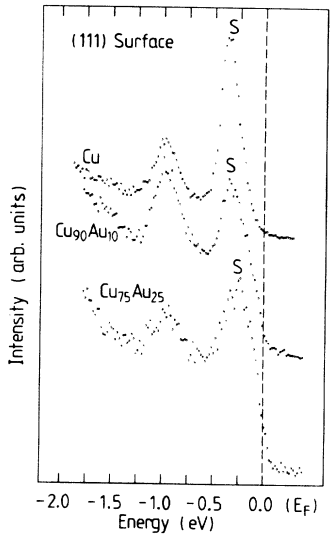

FIG. 6. He I excited normal-emission spectra for the (111) surface to show the $\bar{\Gamma}$-centered Shockley state S in Cu, $Cu_{90}Au_{10}$, and $Cu_{75}Au_{25}$.

can be gained via Cu and Au bands for an *ordered* fcc lattice of $Cu_{75}Au_{25}$ lattice constant. We have considered such *hypothetical* bands (not shown for brevity) based on the present Cu and Au muffin-tin potentials, and find that the separation between Cu and Au bands of the same symmetry varies widely at different **k** points, indicating a strong **k** and E dependency of the effective disorder parameter in the alloy. In particular, the separation between the top of the Cu and Au d bands around point X is relatively small (compared to the bandwidth); in contrast, at the zone center around point Γ, many of the Cu and Au bands are well separated (e.g., Δ_6, Δ_7).

These observations allow us to understand in simple terms the fact that the complex alloy bands near the top of the Cu band edge in Fig. 3 are virtual-crystal-like, suffering little disorder smearing, but that bulk electronic states in many other parts of the Brillouin zone are better described as being in the split-band regime, giving separate Cu- and Au-derived levels, which undergo large disorder smearing.

We find that the Fermi surface (FS) in $Cu_{75}Au_{25}$ continues to be Cu-like showing little change in its major radii. This is to be expected, since Cu and Au possess the same valence, and the FS arises from a virtual crystal-like common *s-p* band [Fig. 3(a)]; the alloy FS would therefore be insensitive to disorder and composition. The present calculations predict a 5.0% decrease in the radius of the L neck.[32] We are not aware of any measurement of the FS radii in disordered CuAu alloys. In ordered $Cu_{75}Au_{25}$, Ref. 33 reports an 8% decrease in the L-neck radius.

Figure 6 shows the (111) Shockley surface-state feature S in Cu and CuAu alloys. We estimate that, compared to Cu, this surface state experiences a shift of 80 meV towards the Fermi energy, and an increased broadening (FWHM) of about 140 meV in the 25% Au alloy; for 10% Au on the other hand, there is no shift in the position of S, and an increased broadening of 70 meV. We have previously been able to obtain a semiquantitative understanding of changes in the Shockley- as well as Tamm-type surface states in several alloys by examining the behavior of the pertinent bulk energy levels.[23] In particular, the (111) Shockley state lies in the projected bulk energy-band L_{6^+}-L_{6^-} gap [Fig. 3(a)]. In the 25% alloy, L_{6^-}, which is the bulk level closest to the surface state, shows no shift and possesses a broadening of only 35 meV; L_{6^+} is lowered by 0.3 eV towards the Fermi level, and broadened by 160 meV. While the average broadening of the L_{6^+} and L_{6^-} levels in the alloy is of the same order of magnitude as the measured value, the observed shift in the position of this surface state does not appear to follow these bulk levels. The interpretation of the surface-state measurements in CuAu may be complicated by the presence of a substantial Au enrichment in the topmost surface layer.

ACKNOWLEDGMENTS

It is a pleasure to acknowledge important discussions with and technical assistance of Mr. A. Vuoristo, Dr. H. Asonen, and Dr. C. Barnes. We are grateful to Professor M. Pessa for support and encouragement. This project is supported by the Academcy of Finland, a travel grant under the U.S.-Finland Program of the U.S. National Science Foundation (NSF), and the U.S. Department of Energy Contract No. ER45223, and benefited from the allocation of supercomputer time on the ER-Cray at Lawrence Livermore National Laboratory (LLNL) and the San Diego Supercomputer Center. Acknowledgment is made to the donors of The Petroleum Research Fund, administered by the American Chemical Society (ACS), for partial support of this research. One of us (E.A.) is indebted to the Tampere Science Foundation and to the Tampere Research Foundation for research grants.

APPENDIX A: SYMMETRY PROPERTIES OF CPA t MATRIX

The formulation of the relativistic KKR-CPA theory proceeds along the lines of the nonrelativistic theory.[25,27] We briefly discuss the symmetry properties of the CPA t matrix $t_{\rm CP}$ arising from the symmetry of the crystal lattice in the double point group O_h.

Details of double-group operators on bispinors are discussed in Ref. 34. The symmetrized bispinor basis states for the irreducible unitary representation $\Gamma^{(i)}$ of dimensionality l_i of the double group can be constructed as

$$\Psi_j^{(i,\kappa)}(\mathbf{r})=\begin{bmatrix} j_l(pr)\chi_j^{(\kappa)}(\mathbf{r}) \\ \dfrac{iS_\kappa pc}{W+mc^2} j_{\bar{l}}(pr)\chi_j^{(-\kappa)}(\mathbf{r}) \end{bmatrix}^{(i)}, \tag{A1}$$

where $\chi_j^{(\kappa)}(\mathbf{r})$ are the symmetrized 2×1 spinors[35] for the Schrödinger-Pauli equation giving the same irreducible representation $\Gamma^{(i)}$. The label j numbers the l_i orthogonal basis states, j_l is a spherical Bessel function, and much of the other notation is conventional and obvious. The matrix elements of $t^{\rm CP}$ in this representation are

$$t^{\rm CP}_{i\kappa j;i'\kappa' j'}(r,r')=\iint [\Psi_j^{(i,\kappa)}(\mathbf{r})]^\dagger t^{\rm CP}(\mathbf{r},\mathbf{r}')[\Psi_{j'}^{(i',\kappa')}(\mathbf{r}')]d\Omega_r\, d\Omega_{r'}\,. \tag{A2}$$

The invariance of $t^{\rm CP}(\mathbf{r},\mathbf{r}')$ under the point-group coordinate operations implies the relation

$$t^{\rm CP}_{i\kappa j;i'\kappa' j'}(r,r')=N_g^{-1}\sum_P \iint \{[P]\Psi_j^{(i,\kappa)}(\mathbf{r})\}^\dagger t^{\rm CP}(\mathbf{r},\mathbf{r}')\{[P]\Psi_{j'}^{(i',\kappa')}(\mathbf{r}')\}d\Omega_r\, d\Omega_{r'}\,, \tag{A3}$$

where the summation runs over all the operators $[P]$ of the double point group[36] of order N_g. Applying the great

orthogonality theorem for unitary matrix elements, as in Ref. 37, Eq. (A3) can be rewritten as

$$t^{\mathrm{CP}}_{i\kappa;i'\kappa'j'}(r,r')=(1/l_i)\delta_{ii'}\delta_{jj'}f^{(i,\kappa,\kappa')}_{\mathrm{CP}}(r,r') \ , \tag{A4a}$$

where

$$f^{(i,\kappa,\kappa')}_{\mathrm{CP}}(r,r')=\sum_{m=1}^{l_i}\int\{\Psi^{(i,\kappa)}_m(\mathbf{r})\}^{\dagger}t^{\mathrm{CP}}(\mathbf{r},\mathbf{r}')\{\Psi^{(i,\kappa')}_m(\mathbf{r}')\}d\Omega_r\,d\Omega_{r'} \ . \tag{A4b}$$

If only s, p, and d valence states are considered, the symmetrized basis of Eq. (A1) for a cubic lattice leads to seven linearly independent elements restricted by the summation in Eq. (A4b), and $\delta_{ii'}\delta_{jj'}$ in Eq. (A4a). Six of these terms occur at the diagonal sites, each corresponding to the following six representations listed below:

$$\kappa=-1(s_{1/2})\rightarrow\Gamma^{6^+} \ ,$$

$$\kappa=1(p_{1/2})\rightarrow\Gamma^{6^-} \ ,$$

$$\kappa=-2(p_{3/2})\rightarrow\Gamma^{8^-} \ ,$$

$$\kappa=2(d_{3/2})\rightarrow\Gamma^{8^+} \ ,$$

$$\kappa=-3(d_{5/2})\rightarrow\Gamma^{7^+},\Gamma^{8^+} \ ,$$

As the representation Γ^{8^+} occurs for both $\kappa=2$ and $\kappa=-3$, there is an additional spin-flip term occuring at eight off-diagonal sites. The results in the (Q,Q') representation are summarized in Table I, and differ from those presented in Ref. 24 in some sign changes.

APPENDIX B: A METHOD FOR SOLVING THE KKR-CPA EQUATION

A major part of the effort in evaluating physical properties in the theory involves obtaining solutions of the KKR-CPA self-consistency equation

$$\tau^{-1}_{\mathrm{CP}}=x\tau^{-1}_A+(1-x)\tau^{-1}_B+(\tau^{-1}_{\mathrm{CP}}-\tau^{-1}_A)T^{\mathrm{CP}}_{00}(\tau^{-1}_{\mathrm{CP}}-\tau^{-1}_B) \ , \tag{B1}$$

where $\tau_{A\,(B)}$ and τ_{CP} are on-the-energy-shell elements of the $A\,(B)$ atom, and the effective CPA t matrices, respectively, and the quantity T_{00} is given by the Brillouin-zone sum

$$T^{\mathrm{CP}}_{00}=\frac{1}{N}\sum_{\mathbf{k}}[\tau^{-1}_{\mathrm{CP}}-B_{\mathbf{k}}(E)]^{-1} \ . \tag{B2}$$

TABLE I. The symmetry-imposed structure of the CPA effective scattering matrix τ_{CP} in QQ' representation. Among the 11 distinct elements shown, the following relationships exist: $g=\frac{1}{5}f+\frac{4}{5}e$, $j=(\frac{1}{5})^{1/2}(e-f)$, $k=(\frac{1}{6})^{1/2}h$, and $l=(\frac{5}{6})^{1/2}h$.

$\kappa\mu$; $\kappa'\mu'$	(-1,0.5)	(-1,-0.5)	(1,0.5)	(1,-0.5)	(-2,1.5)	(-2,0.5)	(-2,-0.5)	(-2,-1.5)	(2,1.5)	(2,0.5)	(2,-0.5)	(2,-1.5)	(-3,2.5)	(-3,1.5)	(-3,0.5)	(-3,-0.5)	(-3,-1.5)	(-3,-2.5)
(-1,0.5)	a																	
(-1,-0.5)		a																
(1,0.5)			b															
(1,-0.5)				b														
(-2,1.5)					c													
(-2,0.5)						c												
(-2,-0.5)							c											
(-2,-1.5)								c										
(2,1.5)									d				-k				-l	
(2,0.5)										d				h				
(2,-0.5)											d				-h			
(2,-1.5)												d	l			k		
(-3,2.5)												l	g			j		
(-3,1.5)									-k					f			j	
(-3,0.5)										h					e			
(-3,-0.5)											-h					e		
(-3,-1.5)												k	j				f	
(-3,-2.5)									-l					j				g

It is shown in Appendix A above that, in a lattice with cubic symmetry, if the quantum number κ is limited to the values $\{\pm 1, \pm 2, -3\}$, then matrices such as $\tau_{\rm CP}^{-1}$ (or $\tau_{\rm CP}$) and $T_{00}^{\rm CP}$ possess only seven basic elements. Hence by defining a seven-dimensional vector $\mathbf{x}$, the components of which are these basic elements of $\tau_{\rm CP}^{-1}$, the CPA equation (B1) can be cast into the form of the mapping

$$\mathbf{x}=\mathbf{f}(\mathbf{x}) , \tag{B3}$$

whose solutions can be found by iterating the multidimensional Newton-Raphson formula

$$\mathbf{x}^{(i+1)}=\mathbf{x}^{(i)}+\alpha\left[1-\left[\frac{\partial \mathbf{f}}{\partial \mathbf{x}}\right]_{\mathbf{x}=\mathbf{x}^{(i)}}\right]^{-1}[\mathbf{f}(\mathbf{x}^{(i)})-\mathbf{x}^{(i)}] , \tag{B4}$$

where a scaling factor α, lying between 0 and 1, has been introduced.

It is straightforward to show that the Jacobian matrix $\partial f/\partial x$ can be manipulated into the form

$$\left[\frac{\partial \mathbf{f}}{\partial \mathbf{x}}\right]_{lm} \equiv \frac{\partial f_l}{\partial x_m} = \left[-(\tau_{\rm CP}^{-1}-\tau_A^{-1})\left[\sum_k (\tau_{\rm CP}^{-1}-B_{\mathbf{k}})^{-1} I_m (\tau_{\rm CP}^{-1}-B_{\mathbf{k}})^{-1}\right](\tau_{\rm CP}^{-1}-\tau_B^{-1})\right]_{K(l)L(l)}$$
$$+[(\tau_{\rm CP}^{-1}-\tau_A^{-1})T_{00}I_m + I_m T_{00}(\tau_{\rm CP}^{-1}-\tau_B^{-1})]_{K(l)L(l)} , \tag{B5}$$

where K and L are the appropriate matrix indices corresponding to the lth element of the seven-component vector (see Table I), and the matrix I_m is defined by the equation

$$I_m = \frac{\partial \tau_{\rm CP}^{-1}}{\partial x_m} . \tag{B6}$$

The iteration procedure based on Eqs. (B4) and (B5) properly treats the coupling between various elements of $\tau_{\rm CP}$, and we find that it often leads to an order-of-magnitude improvement in convergence over the single-element methods. In fact, in regions of large disorder scattering the single-element methods may not converge at all. Note, however, that the multicomponent method involves additional $\mathbf{k}$-space integrations, as seen from Eq. (B5).

[1]W. Scott and L. Muldawer, Phys. Rev. B **9**, 1115 (1974); R. J. Nastasi-Andrews and R. E. Hummel, *ibid.* **16**, 4314 (1977).

[2]P.-O. Nilsson and C. Norris, Phys. Lett. **29A**, 22 (1969).

[3]Z. Q. Wang, S. C. Wu, J. Quinn, C. K. C. Lok, Y. S. Li, F. Jona, and J. W. Davenport, Phys. Rev. B **38**, 7442 (1988).

[4]R. G. Jordan and G. S. Sohal, J. Phys. C **15**, L663 (1982).

[5]A. R. von Neida and R. B. Gordon, Philos. Mag. **7**, 1129 (1962).

[6]G. Airoldi and M. Drosi, Philos. Mag. **19**, 349 (1969); G. Airoldi, M. Asdente, and E. Rimini, *ibid.* **10**, 43 (1964).

[7]I. Lindau and L. Walldén, Solid State Commun. **9**, 209 1147 (1971).

[8]E. G. McRae and R. A. Malic, Surf. Sci. **148**, 551 (1984).

[9]V. Kumar and K. H. Bennemann, Phys. Rev. Lett. **53**, 278 (1984).

[10]V. S. Sundaram, R. S. Alben, and W. D. Robertson, Surf. Sci. **46**, 653 (1974).

[11]T. M. Buck , G. H. Wheatley, and L. Marchut, Phys. Rev. Lett. **51**, 43 (1983).

[12]T. M. Buck, in *Chemistry and Physics of Solid Surfaces IV,* edited by R. Vanselow and R. Howe (Springer-Verlag, Berlin, 1982), p. 435.

[13]C. G. Shaw and S. C. Fain, Jr., in *Proceedings of the Seventh International Vacuum Congress and the Third International Conference on Solid Surfaces, Vienna, 1977,* edited by R. Dobrozemsky *et al.* (Berger, Vienna, 1977), p. 2315.

[14]W. Eberhardt, S. C. Wu, R. Garrett, D. Sondericker, and F. Jona, Phys. Rev. B **31**, 8285 (1985).

[15]S. B. Di Cenzo, P. H. Citrin, E. H. Hartford, Jr., and G. K. Wertheim, Phys. Rev. B **34**, 1343 (1986).

[16]G. K. Wertheim, L. F. Mattheiss, and D. N. E. Buchanan, Phys. Rev. B **38**, 5988 (1988).

[17]D. Gray and E. Brown, Phys. Rev. **160**, 567 (1967); H. L. Skriver and H. P. Lengkeek, Phys. Rev. B **19**, 900 (1979).

[18]R. G. Jordan, G. S. Sohal, B. L. Gyorffy, P. J. Durham, W. M. Temmerman, and P. Weinberger, J. Phys. F **15**, L135 (1985).

[19]J. W. Davenport, R. E. Watson, and M. Weinert, Phys. Rev. B **37**, 9985 (1988).

[20]P. Weinberger, A. M. Boring, R. C. Albers, and W. M. Temmerman, Phys. Rev. B **38**, 5357 (1988).

[21]B. Ginatempo and J. B. Staunton, J. Phys. F **18**, 1827 (1988).

[22]H. Asonen, C. J. Barnes, M. Pessa, R. S. Rao, and A. Bansil, Phys. Rev. B **31**, 3245 (1985).

[23]H. Asonen, M. Lindroos, M. Pessa, R. Prasad, R. S. Rao, and A. Bansil, Phys. Rev. B **25**, 7075 (1982); A. Bansil, R. S. Rao, R. Prasad, H. Asonen, and M. Pessa, J. Phys. F **14**, 273 (1984); R. S. Rao, A. Bansil, H. Asonen, and M. Pessa, Phys. Rev. B **29**, 1713 (1984); R. S. Rao and M. Pessa, in *Electronic Band Structure and its Applications,* edited by M. Yussouff (Springer-Verlag, Berlin, 1987).

[24]J. Staunton, B. L. Gyorffy, and P. Weinberger, J. Phys. F **10**, 2665 (1980); G. M. Stocks and H. Winter, in *The Electronic Structure of Complex Systems,* edited by P. Phariseau and W. M. Temmerman (Plenum, New York, 1984); see also the article by P. J. Durham in this volume.

[25]H. Ehrenreich and L. Schwartz, in *Solid State Physics,* edited by H. Ehrenreich, F. Seitz, and D. Turnbull (Academic, New York, 1976), Vol. 31.

[26]A. Bansil, R. S. Rao, P. E. Mijnarends, and L. Schwartz, Phys. Rev. B **23**, 3608 (1981).

[27]For a recent review, see A. Bansil, in *Electronic Band Structure and its Applications,* edited by M. Yussouff (Springer-

Verlag, Berlin, 1987), p. 273.

[28]Assuming a free-electron *final-state* band (valid for radiation frequencies considered in this work), the final-state $\mathbf{k}$ vector can be expressed as $|\mathbf{k}^f|=[(2m^*)^{1/2}/\hbar](E_k-V_0)^{1/2}$, where E_K is the kinetic energy of the electron outside the crystal. The inverse effective mass $1/m^*$ is taken here as the weighted average of the inverses of pure Cu and Au effective masses of $0.90m_e$ and $1.16m_e$, respectively, obtained from Refs. 23 and 29. The inner potential V_0 is then evaluated semiempirically by using the computed complex bands to obtain the $\mathbf{k}^f$ value for the Ne I excited photoemission peak at -1.40 eV of the (100) surface spectra. Note that the error in evaluating the $\mathbf{k}^f$ is small for this peak due to high dispersion of the *initial-state sp* band. The simplified method of evaluating the $\mathbf{k}^f$ values from the observed photoemission peaks, described above, has been used extensively in the literature (Refs. 3 and 23).

[29]R. Courths, H. Wern, U. Hau, B. Cord, V. Bachelier, and S. Hüfner, J. Phys. F **14**, 1559 (1984).

[30]Also, at the He II excitation energy, Figs. 1(b) and 2(b), photoemission is especially dominated by contribution from the surface region due to the short electron mean free path; as in our previous studies, He II spectra are not sensible to use in deducing disorder-induced broadenings.

[31]FWHM have been estimated as in our previous studies (Refs. 22 and 23).

[32]For comparison, in $Cu_{70}Zn_{30}$, the neck radius increases by about 70%, and the (100)-belly radius by 7%; see R. Prasad, S. C. Papadopoulos, and A. Bansil, Phys. Rev. B **23**, 2607 (1981).

[33]P. P. Deimel, R. J. Higgins, and R. K. Goodall, Phys. Rev. B **24**, 6197 (1981); P. P. Deimel and R. J. Higgins, *ibid.* **25**, 7117 (1982).

[34]D. F. Johnston, Proc. R. Soc. London, Ser. A **243**, 546 (1958).

[35]Y. Onodera and M. Okazaki, J. Phys. Soc. Jpn. **21**, 2400 (1966).

[36]There are two members in the double group for each coordinate transformation generally referred to as *unbarred* and *barred* operators, and the summation in Eq. (A3) runs over the *barred* as well the *unbarred* operators. The labeling $\Gamma^{(i)}$ as in Ref. 35.

[37]A. Bansil, Phys. Rev. B **20**, 4025 (1979).

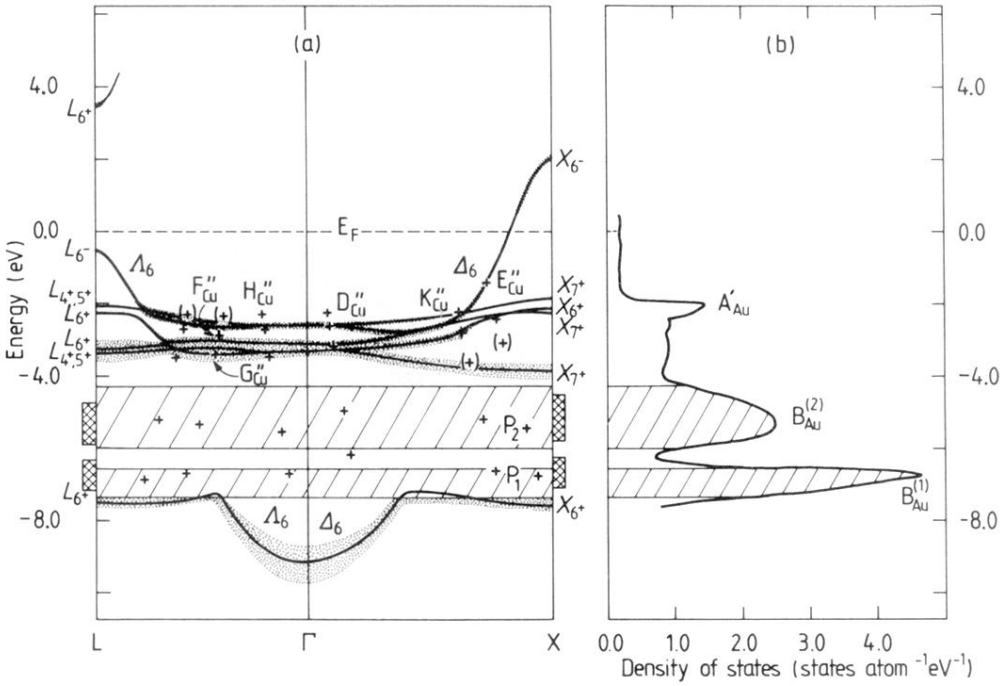

FIG. 3. (a) Relativistic KKR-CPA complex energy bands along the symmetry directions $\Gamma-X$ and $\Gamma-L$, and (b) Au-component density of states in $Cu_{75}Au_{25}$. Disorder smearing of energy bands is represented by the vertical length of shading, which is twice the imaginary part of the complex energy. Heavily smeared Au-related d bands are shown in (a) by hatched regions of FWHM of the corresponding relativistically split peaks, $B^{(1)}_{Au}$ and $B^{(2)}_{Au}$, in the Au-component density of states in (b). Crosses denote the $E(\mathbf{k})$ values obtained from the experimental spectra (labels are keyed to the features of Figs. 1 and 2); parentheses indicate that the corresponding transitions in the spectra are seen only as shoulders. Cross-hatched regions on either sides of (a) estimate the average position and FWHM of the Au-derived structures in the ARPES spectra. Peak A'_{Au} in Au-component density of states is discussed in the text.

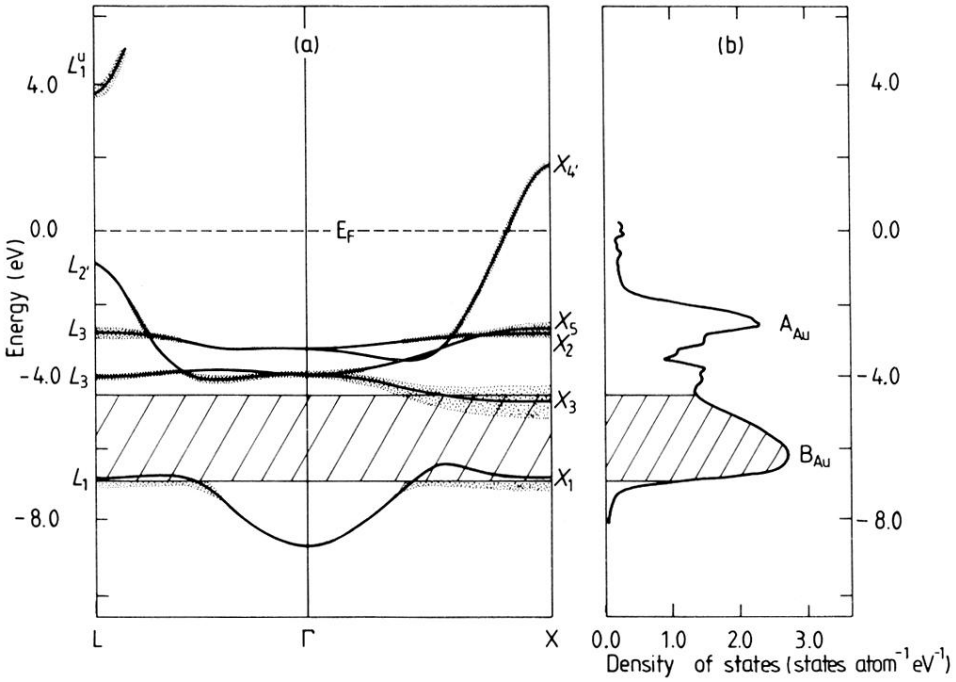

FIG. 4. (a) Nonrelativistic KKR-CPA complex energy bands along the symmetry directions Γ–X and Γ–L, and (b) Au-component density of states in $Cu_{75}Au_{25}$. Cu and Au potentials used in these calculations are the same as those in the relativistic computations of Fig. 3.